

Anisotropy Characteristics of Exposed Gravel Beds Revealed in High-Point-Density Airborne Laser Scanning Data

Guo-Hao Huang, Chi-Kuei Wang, Fu-Chun Wu, and Peter M. Atkinson

Abstract—The aim of this study was to examine the relationship between the anisotropy direction of exposed gravel bed and flow direction. Previous studies have shown that the anisotropy direction of a gravel bed surface can be visually determined in the elliptical contours of 2-D variogram surface (2DVS). In this letter, airborne laser scanning (ALS) point clouds were acquired at a gravel bed, and the whole data set was divided into a series of $6\text{ m} \times 6\text{ m}$ subsets. To estimate the direction of anisotropy, we proposed an ellipse-fitting-based automatic procedure with consideration given to the grain size characteristic d_{50} to estimate the primary axis of anisotropy [hereafter referred to as the primary continuity direction (PCD)] in the 2DVS. The ALS-derived PCDs were compared to the flow directions (for both high and low flow) derived from hydrodynamic model simulation. Comparison of ALS-derived PCDs and simulated flow directions suggested that ALS-derived PCDs could be used to infer flow direction at different flow rates. Furthermore, we found that the ALS-derived PCDs estimated from any elliptical contour of the 2DVS exhibited a similar orientation when the contours of the 2DVS reveal the clear anisotropic structure, demonstrating the robustness of the technique.

Index Terms—Airborne laser scanning (ALS), flow direction, spatial continuity, 2-D variogram surface (2DVS).

I. INTRODUCTION

THE geostatistical variogram function has been recognized as an important tool for detecting spatial anisotropy in different variables, such as air pollution [1], snow depth [2], and exposed gravel bed structures [3]–[8]. The anisotropy indicates that the spatial correlation pattern changes with orientation, and it can be represented by the elliptical contours in a 2-D variogram surface (2DVS).

Many studies have shown that the visually determined anisotropy direction of a 2DVS can be associated with different mechanisms, such as wind for air pollution and snow depth structures [1], [2] and hydrodynamic dispersion (i.e., flow

movement) for homogeneous porous media [9]. In the last two decades, substantial studies have investigated the anisotropy directions derived from a 2DVS in the exposed gravel beds and suggested that the anisotropy directions exhibited in the gravel bed surfaces reflect the dominant grain orientation [3]–[6]. Various studies have examined the relationship between gravel orientation and flow direction [10]–[16]. For lower flows, larger pebbles, and lower pebble concentrations, elongated pebbles are transported by rolling and are deposited with their major axes normal to the flow direction. For higher flows, smaller pebbles, and higher pebble concentrations, the pebbles skip along the bed and tend to be deposited with their major axis parallel to the flow [16]. It has been reported that particle imbrication would occur naturally in a direction parallel to the flow [5], [16], [17]. Particle imbrication covering a range of directions might indicate that flow direction changed over the duration of the last competent event (e.g., varied with flow depth) or that different flows (with different directions) imbricated particles in different ways over time [16]. It has also been reported that the anisotropy directions failed at being conclusive on the surface-forming flow direction [5], [18]. The latter is notoriously difficult to determine accurately from *in situ* visual observations [19].

The determination of flow direction is essential to trace the water paths and sediment transportation. For coarse bed materials, rolling/sliding and saltation are the most possible modes of sediment transport, with rolling/sliding dominated by coarser pebbles and saltation dominated by finer gravel. Alignment of bed particles transverse to the flow can be associated with transport mode by rolling and sliding [17], while bed structure longitudinal to the flow can be attributed to deposition of saltating particles after contact with the upstream front of stable grain and particle imbrications [4], [5], [20]. It is thus of interest to explore the relationship between the anisotropy of gravel bed surfaces and flow direction across large areas. However, comparison of anisotropy direction determined visually from a 2DVS, extracted for laboratory and field gravel surfaces, to flow direction determined from subjective observation [3]–[6] revealed no common consensus about the relationship between anisotropy direction and flow movement in exposed gravel beds. This is possibly due to the limited numbers of data and the small spatial extents available to earlier researchers.

Advances in remote sensing have facilitated the measurement of gravel bed surfaces in a spatially extensive and cost-effective way based on the airborne approach, including airborne laser scanning (ALS), aerial photogrammetry, and unmanned aerial systems (UASs) [8], [21]–[23]. Huang and Wang [8] have indicated that a detailed description of gravel bed surfaces is

Manuscript received November 8, 2015; revised March 16, 2016 and April 11, 2016; accepted April 27, 2016.

G.-H. Huang and C.-K. Wang are with the Department of Geomatics, National Cheng Kung University, Tainan 70101, Taiwan (e-mail: chikuei@mail.ncku.edu.tw).

F.-C. Wu is with the Department of Bioenvironmental Systems Engineering, National Taiwan University, Taipei 10617, Taiwan.

P. M. Atkinson is with the Department of Geography and Environment, University of Southampton, SO17 1BJ Southampton, U.K., with the Faculty of Science and Technology, Lancaster University, Lancaster LA1 4YW, U.K., with the Faculty of Geosciences, University of Utrecht, 3584 Utrecht, The Netherlands, and also with the School of Geography, Archaeology and Palaeoecology, Queen's University, Belfast BT7 1NN, U.K.

Color versions of one or more of the figures in this paper are available online at <http://ieeexplore.ieee.org>.

Digital Object Identifier 10.1109/LGRS.2016.2562061

88 a prerequisite for visualizing the obvious anisotropy pattern in
 89 the 2DVS of gravel bed surfaces. Recent progress on combining
 90 UAS and structure-from-motion photogrammetry has gained
 91 attention for measuring submerged and dry gravel beds, and
 92 it has been shown that a digital elevation model (DEM) with
 93 a spatial resolution of a few centimeters can be achieved [22],
 94 [23]. However, the UAS has to be operated at a low altitude
 95 (i.e., lower than 100 m) for such a purpose, and this would be
 96 challenging when performing UAS surveys in river valleys. The
 97 ALS, which incorporates laser ranging, inertial measurement
 98 unit, and Global Positioning System technologies, has shown
 99 potential for mapping the surface elevation of a large area [24].
 100 Moreover, the pulse repetition frequencies of the commercial
 101 ALS systems have increased from 70 kHz in 2003 (as for the
 102 ALS used in this study) to 900 kHz in 2014 [25], which shows
 103 that the ALS is now economically favorable for capturing
 104 gravel bed surfaces with high-density ALS point clouds.

105 In this research, we examined the anisotropy characteristics
 106 of a very high-point-density ALS data of an exposed gravel
 107 bed by comparing its anisotropy direction with simulated flow
 108 directions under high- and low-flow scenarios based on fixed-
 109 bed hydrodynamic modeling. To better reveal the variation of
 110 the anisotropy characteristic within the river channel, the whole
 111 ALS data set was divided into a series of $6\text{ m} \times 6\text{ m}$ subsets,
 112 which results in 324 subsets of ALS point data. In order to
 113 consistently derive the anisotropy direction for each $6\text{ m} \times 6\text{ m}$
 114 subset, we devised an ellipse-fitting-based automatic procedure
 115 with the consideration of the grain size characteristic d_{50} , which
 116 is the median of particle size distribution, to determine the
 117 primary axis of anisotropy [hereafter, referred to as the primary
 118 continuity direction (PCD)] in the 2DVS.

119 II. METHOD

120 A. 2DVS

121 The variogram has been used widely to quantify the spatial
 122 variability in gravel bed surfaces [4], [5], [8]. The empirical
 123 variogram, which is half the mean squared difference between
 124 pairs of data points separated by the lag vector \mathbf{h} , can be
 125 expressed as

$$\hat{\gamma}(\mathbf{h}) = \frac{1}{2N(\mathbf{h})} \sum_{i=1}^{N(\mathbf{h})} [z(\mathbf{x}_i) - z(\mathbf{x}_i + \mathbf{h})]^2 \quad (1)$$

126 where $\hat{\gamma}(\mathbf{h})$ is the semivariance, the lag (distance and direction)
 127 vector \mathbf{h} is the separation between two data points, $N(\mathbf{h})$ is the
 128 number of point pairs separated by lag \mathbf{h} , and $z(\mathbf{x}_i)$ is the bed
 129 elevation at the location \mathbf{x}_i .

130 The empirical variogram is a function that relates semivari-
 131 ance $\hat{\gamma}(\mathbf{h})$ to lag \mathbf{h} and is usually expressed as a set of 1-D plots,
 132 where different plots represent different directions. An alterna-
 133 tive is to plot all directions together as a 2DVS, i.e., a raster map
 134 of semivariance values $\hat{\gamma}(\mathbf{h}_x, \mathbf{h}_y)$ representing the empirical
 135 variogram for all available lag vectors $\mathbf{h} = (\mathbf{h}_x, \mathbf{h}_y)$ [1], [26].

136 Previous studies suggested the removal of possible large-
 137 scale topographic trends (i.e., the bed slope), which causes the
 138 spatial basis in the collected spatial data, before calculation
 139 of the 2DVS [5]. In this research, the planar detrending was
 140 applied to each ALS $6\text{ m} \times 6\text{ m}$ subset, and the elevation
 141 residuals were used for calculation of the 2DVS.

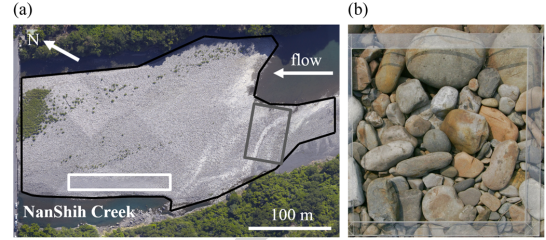


Fig. 1. (a) Georectified orthophoto with a spatial resolution of $5\text{ cm} \times 5\text{ cm}$ showing the gravel bar near the confluence of the NanShih Creek and PeiShih Creek, northern Taiwan, with a latitude of $24^\circ 54' 10''$ N and longitude of $121^\circ 33' 24''$ E. The black polygon shows the extent of exposed gravel bed. The gray rectangle represents a temporally submerged area caused by daily discharge fluctuations. The white rectangle represents an area that is covered by silt and gravel. (b) Image taken from the $50\text{ cm} \times 50\text{ cm}$ acrylic frame for photo-sieving.

B. Automatic Determination of Anisotropy Direction by Ellipse Fitting 142 143

The 2DVS expressed as a contour plot can facilitate the
 analysis of spatial continuity (i.e., spatial autocorrelation) by
 visualizing the spatial variability along all directions simultane-
 ously [1], [26]. It is thus suggested that the anisotropy direction
 can be determined by tracing one of the elliptical contours in
 the 2DVS [26]. 144 145 146 147 148 149

The procedure for determining the PCD is described as fol-
 lows. First, because the magnitude of the contours of the 2DVS
 is influenced by the actual semivariances $\hat{\gamma}(\mathbf{h}_x, \mathbf{h}_y)$, the semi-
 variances $\hat{\gamma}(\mathbf{h}_x, \mathbf{h}_y)$ in the 2DVS were standardized (divided by
 the variance of the elevation residuals for each ALS $6\text{ m} \times 6\text{ m}$
 subset), which implies that the contour levels in the 2DVS range
 theoretically between 0 and just greater than 1 (the maximum
 theoretical value is equal to the *a priori* variance not the sample
 variance). Then, we applied an ellipse-fitting procedure to all
 elliptical contours of the 2DVS such that the PCD, which rep-
 resents the direction of greatest spatial continuity (i.e., spatial
 autocorrelation), is estimated as the direction of the major axis
 of the fitted ellipse. Since the number of available contour levels
 in the 2DVS is inherently affected by the spatial autocorrelation
 property of the subject under investigation (in our case, the ALS
 point cloud of a exposed gravel bed), this raises difficulties in
 choosing the contour with a specific contour level for each ALS
 $6\text{ m} \times 6\text{ m}$ subset. As a result, the PCD is determined when the
 semimajor length of fitted ellipses falls in a given range derived
 by the grain size characteristic d_{50} . We chose the d_{50} value
 as a physically based guidance in the ellipse-fitting procedure,
 rather than an arbitrary measurement value, with the hope to
 maximize the transferability of this procedure to other study
 areas. The test results for determining the range constraint are
 shown in section *Determination of ALS-derived PCDs*. 150 151 152 153 154 155 156 157 158 159 160 161 162 163 164 165 166 167 168 169 170 171 172 173 174

175 III. DATA

The study area [Fig. 1(a)] is an exposed gravel bed (denoted
 as the black polygon) near the confluence of the NanShih
 Creek and PeiShih Creek, northern Taiwan, with latitude and
 longitude of $24^\circ 54' 10''$ N and $121^\circ 33' 24''$ E, respectively. The
 gravel bed was occasionally submerged and migrated by severe
 floods caused by typhoons that occurred between May and
 November of each year. It is noted that low discharges would
 temporarily cause a submerged area, which is denoted by the
 gray rectangle in Fig. 1(a). 176 177 178 179 180 181 182 183 184

185 Fig. 1(b) shows one of the 22 image samples, which were
 186 taken from the 50 cm \times 50 cm acrylic frame in the exposed
 187 gravel bed in Fig. 1(a). We applied the photo-sieving technique
 188 developed by Graham *et al.* [27] to derive the particle size
 189 distribution aggregated from the 22 image samples, and the
 190 resultant d_{50} is equal to 5.5 cm.

191 A. ALS

192 An ALS survey was conducted on May 7, 2009, at the above
 193 ground level of 650 m along the river channel using an Optech
 194 ALTM 3070 system onboard a helicopter with nominal eleva-
 195 tion and horizontal accuracies of 15 and 32.5 cm, respectively.
 196 The average point cloud density was 247 pts \cdot m $^{-2}$. Further-
 197 more, aerial photographs were also collected by a medium-
 198 format digital camera, integrated with an Optech ALTM 3070,
 199 simultaneously with laser scanning in order to generate georec-
 200 tified orthophotos with a spatial resolution of 5 cm \times 5 cm, as
 201 shown in Fig. 1(a).

202 For the ALS data of the exposed gravel bed, first, the extreme
 203 high points were removed manually. Then, the whole point data
 204 were divided into a series of 6 m \times 6 m subsets, each of which
 205 was aligned with the longitudinal and transverse directions in
 206 the mainstream of NanShih Creek. The mean spacing between
 207 the centers of 6 m \times 6 m subsets is 8 m. The specific 6 m \times 6 m
 208 subset size was chosen because our previous study [8] demon-
 209 strated that, using this size, reliable anisotropy patterns can
 210 be obtained for each subset while maximizing the number of
 211 available subsets. Furthermore, in order to avoid the potential
 212 bias caused by vegetation (sparse and short *Miscanthus*) on the
 213 gravel bed, we calculated the 2DVSs of ALS 6 m \times 6 m data
 214 sets only where the cumulative vegetation area was smaller than
 215 1 m 2 with the help of the 5-cm resolution orthophoto. This leads
 216 to 324 subsets available for 2DVS calculation.

217 The ALS data are also used to produce the DEM of the dry
 218 surfaces within the study area with a resolution of 1 m \times 1 m,
 219 where the point clouds belonging to vegetation were removed
 220 by visual inspection in Terrscan environment. Due to the in-
 221 frared wavelength of 1064 nm operated by the ALTM 3070,
 222 water absorption prevents ALS measurement for underwater
 223 surfaces. The underwater elevations were thus measured using
 224 a total station and surveying prism pole in wadable areas, while
 225 a shipboard single-beam SONAR was used to survey deeper
 226 areas in June 2009. To facilitate the integration of a complete
 227 DEM of the study area, all surveying, including ALS, was
 228 referenced to TWD97 datum, the national coordinate system
 229 of Taiwan. The DEMs of the wet surfaces of a resolution of
 230 1 m \times 1 m were interpolated from total station and SONAR
 231 data. The complete DEM of the study area was created by
 232 mosaicking the two DEMs of the dry and wet surfaces, respec-
 233 tively, and was further used for hydrodynamic modeling.

234 B. Hydrodynamic Modeling

235 To explore the relation between the ALS-derived PCDs and
 236 flow directions, we simulated the depth-averaged 2-D flow
 237 fields under high- and low-flow scenarios using a finite-element
 238 (FE) hydrodynamic model developed by Wu *et al.* [28]. The
 239 computational domain, extending 600 m to the Hsintien Creek
 240 and 700 and 500 m to the NanShih and PeiShih Creeks
 241 [Fig. 2(a)], contained 17105 elements and 9000 nodes with a

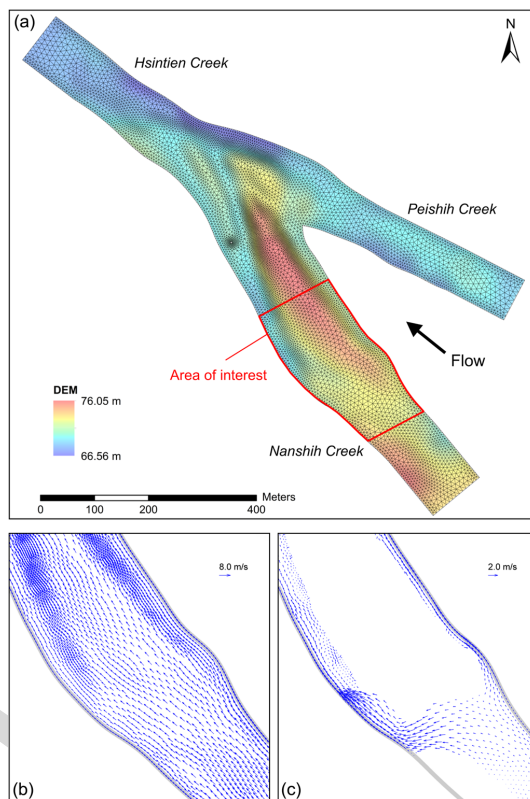


Fig. 2. (a) ALS-derived DEM map and computational mesh of simulation domain, which extends 600 m to the Hsintien Creek and 700 and 500 m to the NanShih and PeiShih Creeks, and contains 17105 elements and 9000 nodes with a mean spacing of 4 m; simulated velocity vectors under (b) high-flow and (c) low-flow scenarios, where the regions without velocity data are exposed bars. The scenario simulations exhibit different extents of bar submergence and distinct patterns of 2-D flow field.

mean spacing of 4 m. The ALS-derived DEM was mapped
 242 to the FE grids via a triangulated irregular network shown in
 243 Fig. 2(a). The model was validated with the observed water lev-
 244 els [29]. The calibrated parameter values were then used for the
 245 scenario simulations. The upstream boundary conditions (BC)
 246 were specified with the flows from the NanShih and PeiShih
 247 Creeks, while the downstream BC was specified with the water
 248 depth at the Hsintien Creek. For the high-flow scenario, the
 249 specified flows (3400 and 1230 m 3 s $^{-1}$) are equivalent to a flood
 250 event with seven-year return period; for the low-flow scenario,
 251 the specified values (23 and 18 m 3 s $^{-1}$) correspond to flows
 252 with a 50% probability of exceedance. These two scenario
 253 simulations exhibited different extents of bar submergence and
 254 distinct patterns of 2-D flow field [Fig. 2(b) and (c)]. The
 255 simulated velocity vectors at the FE nodes were interpolated
 256 to the centers of the 6 m \times 6 m ALS subset, allowing direct
 257 comparisons of the ALS-derived PCDs and flow directions. 258

IV. RESULTS AND DISCUSSION

A. Anisotropy Property of 2DVSs

The 2DVSs of the 324 ALS 6 m \times 6 m subsets were com-
 261 puted using the R software, and the contour map of the 2DVS
 262 was generated using a purpose-written MATLAB program. 263
 264 Based on internal testing, the lag distance of the 2DVS and the
 265 contour level interval in the contour plot were set to 15 cm and
 0.05, respectively, to best reveal anisotropic structures. 266

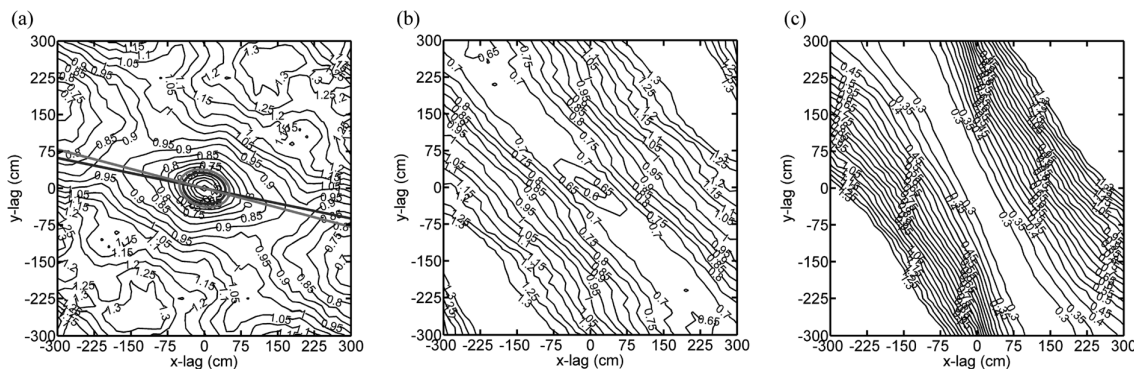


Fig. 3. (a) Contours of the 2DVS reveal a clear anisotropic structure. The ellipse-fitting procedure was applied to the black and gray contour, respectively, in order to determine the PCDs. The black and gray lines are the PCDs determined from the fitted ellipse with the semimajor axis lengths equal to $8.0 d_{50}$ and $9.5 d_{50}$, respectively. The contours of the 2DVS in (b) and (c) show a clear anisotropic structure, but there exist only parallel contours in (c), which prevents application of the ellipse-fitting procedure to obtain the PCD.

267 Most of the 2DVSs of the ALS $6\text{ m} \times 6\text{ m}$ subsets revealed
 268 a clear anisotropic structure similar to the contours shown
 269 in Fig. 3(a). It is thus appropriate to apply the ellipse fitting
 270 procedure to a specific contour to determine the PCD. While a
 271 small number of subsets show fewer [Fig. 3(b)] or no [Fig. 3(c)]
 272 elliptical contours in their 2DVSs, the anisotropic structure is
 273 still prominent. Based on visual inspection, the 2DVSs similar
 274 to Fig. 3(b) and (c) appeared to be in the area covered by silt and
 275 gravel, which is highlighted by the white rectangle in Fig. 1(a).
 276 Due to the requirement of ellipse fitting, the ALS-derived PCDs
 277 are only available for those 2DVSs similar to Fig. 3(a) and (b).

278 B. Determination of ALS-Derived PCDs

279 To mitigate the influence of the jagged appearance of the
 280 elliptical contours with small lag distances [c.f., Fig. 3(a)] on
 281 the PCD estimation, we applied the ellipse-fitting procedure
 282 only to those contour lines including more than 20 cells in the
 283 2DVS, which implies that the semimajor axis length of the fitted
 284 ellipse should be larger than $7 d_{50}$ in our study area.

285 When there are more than two candidate contour lines that
 286 fall in a range of multiple times of d_{50} , we select the PCD
 287 with the smallest semimajor axis length. As shown in our data,
 288 the difference between different PCDs is insignificant. Fig. 3(a)
 289 shows an example for the determination of the PCD with the
 290 semimajor axis length constraint being $7\text{--}10 d_{50}$, and two
 291 candidate contours with their semimajor axis lengths of $8.0 d_{50}$
 292 [black line in Fig. 3(a)] and $9.5 d_{50}$ [gray line in Fig. 3(a)]
 293 were found, where the former one would be reported. The angle
 294 difference between these two PCDs is as small as 3° .

295 To further examine the insignificance of PCD bias caused by
 296 the choice of semimajor axis length constraint in the ellipse fit-
 297 ting, we generated three sets of ALS-derived PCDs determined
 298 from the semimajor axis length within three ranges, i.e., $7\text{--}10 d_{50}$,
 299 $9\text{--}12 d_{50}$, and $11\text{--}14 d_{50}$, and compared these PCD results with
 300 the simulated high- and low-flow directions. The choice of these
 301 constraint ranges was made in order to maximize of chance of
 302 having at least one available contour for each constraint.

303 C. Comparison of ALS-Derived PCDs and Simulated 304 Flow Directions

305 The angle differences of the ALS-derived PCDs and simu-
 306 lated flow directions were calculated. The positive angle dif-

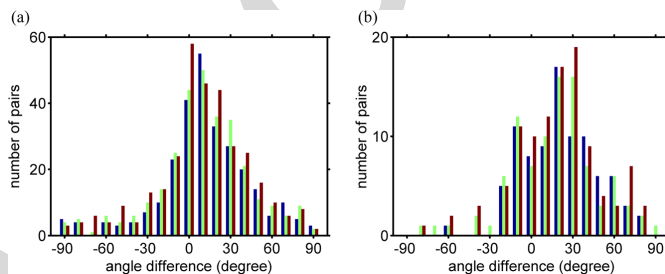


Fig. 4. Histograms of the angle differences between the three sets of ALS-derived PCDs and simulated flow directions at (a) high and (b) low flow. The red, green, and blue bins represent the histograms of the angle differences calculated from the three sets of ALS-derived PCDs determined by the semimajor axis length constraints, which are $7\text{--}10 d_{50}$, $9\text{--}12 d_{50}$, and $11\text{--}14 d_{50}$, respectively.

ferences denote that the ALS-derived PCD lies to the left of
 307 the simulated flow directions when facing downstream; the
 308 negative angle differences denote that the ALS-derived PCD
 309 lies to the right of the simulated flow directions. 310

The histograms of the angle differences for high and low
 311 flow are shown in Fig. 4(a) and (b), respectively. The red,
 312 green, and blue bins in Fig. 4 represent the histograms of the
 313 angle differences calculated from the three sets of ALS-derived
 314 PCDs determined by the semimajor axis length constraints
 315 being $7\text{--}10 d_{50}$, $9\text{--}12 d_{50}$, and $11\text{--}14 d_{50}$, respectively. For the
 316 high flow, the total numbers of comparison pairs are 324, 299, 317
 and 275 when the semimajor axis constraints are $7\text{--}10 d_{50}$, 318
 $9\text{--}12 d_{50}$, and $11\text{--}14 d_{50}$, respectively; for the low flow, the total
 319 numbers of comparison pairs become 107, 96, and 89 when
 320 the semimajor axis constraints are $7\text{--}10 d_{50}$, $9\text{--}12 d_{50}$, and
 321 $11\text{--}14 d_{50}$, respectively. Because the submerged area is much
 322 smaller for low-flow condition [c.f., Fig. 2(c)], the number of
 323 comparison pairs for low flow was much less than that for high
 324 flow. Furthermore, we noted that the number of available ALS-
 325 derived PCDs decreased with the increase of the semimajor
 326 axis length constraint. Because the semivariations of 2DVS are
 327 expected to increase slowly at large lag distances [1], [26],
 328 the larger spacing of contours in the 2DVS leads to fewer
 329 contours available for ellipse fitting. As observed in Fig. 3(a),
 330 the elliptical contours starting from 0.5 to 0.9 become sparse. It
 331 is also noted that the contours became fragmented, and it was
 332 not easy to find ellipse shape [as shown in the upper left and
 333 lower right corner in Fig. 3(a)] when the data are not able to
 334 reveal such long range spatial correlation in the 2DVS. 335

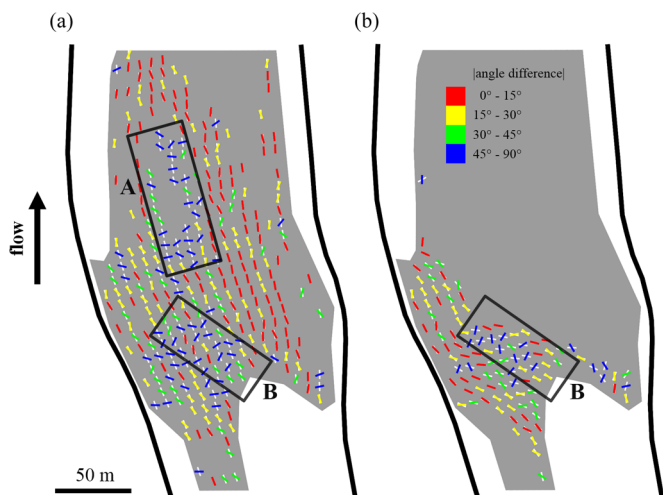


Fig. 5. Comparison of the ALS-derived PCDs and simulated flow directions at (a) high and (b) low flow. The gray polygon is the extent of the exposed gravel bed. The white segments represent the simulated flow directions. The red, yellow, green, and blue segments denote the absolute values of angle difference of $0^\circ-15^\circ$, $15^\circ-30^\circ$, $30^\circ-45^\circ$, and $45^\circ-90^\circ$, respectively, of the ALS-derived PCDs with respect to simulated flow directions. Rectangle A denotes the area with notable discrepancies of ALS-derived PCDs and high-flow direction. Rectangle B denotes the area where the ALS-derived PCDs have better agreement with low-flow direction than high-flow direction.

336 As observed in Fig. 4, the distributions of the angle differ-
 337 ences with three different semimajor axis constraints for high
 338 and low flow are, respectively, similar. To further demonstrate
 339 the similarity between each distribution of angle difference,
 340 for high and low flow, respectively, we applied the nonpara-
 341 metric Kruskal–Wallis test, implemented in R software. The
 342 null hypothesis for the Kruskal–Wallis test is that the three
 343 sets of angle differences come from the same distribution. The
 344 resultant p -values for the Kruskal–Wallis test are 0.89 and 0.83
 345 for high and low flow, respectively, both of which failed to reject
 346 the null hypothesis at the significant level of 0.05. This implies
 347 that the angle differences calculated from the three sets of
 348 ALS-derived PCDs and simulated flow directions do not reveal
 349 statistically significant differences. It is thus suggested that the
 350 ALS-derived PCDs derived from any elliptical contour of the
 351 2DVS should exhibit similar orientation when the contours
 352 of the 2DVS reveal the clear anisotropic structure. The ALS-
 353 derived PCDs determined with the semimajor axis length con-
 354 straint of $7-10 d_{50}$ are discussed as it gave the largest number
 355 of comparison pairs.

356 Fig. 5(a) and (b) demonstrates the comparison of ALS-
 357 derived PCDs and simulated high- and low-flow directions,
 358 respectively. The gray polygon in Fig. 5 shows the extent
 359 of exposed gravel bed [also shown as the black polygon in
 360 Fig. 1(a)]. The white segments in Fig. 5 represent the simulated
 361 flow directions. We observed that the simulated flow directions
 362 for high flow are primarily parallel to the main stream direc-
 363 tion in Fig. 5(a). Moreover, the simulated low flow primarily
 364 flows through the temporarily submerged area in Fig. 5(b)
 365 [c.f., the gray rectangle in Fig. 1(a)]. The red, yellow, green,
 366 and blue segments in Fig. 5 denote the absolute values of
 367 angle difference of $0^\circ-15^\circ$, $15^\circ-30^\circ$, $30^\circ-45^\circ$, and
 368 $45^\circ-90^\circ$, respectively, of the ALS-derived PCDs with respect to simu-
 369 lated flow directions.

We noted a good agreement between the ALS-derived PCDs 370
 and simulated high flow in the right portion of the exposed 371
 gravel bar [Fig. 5(a)], where the white segments become invis- 372
 ible due to the insignificant angle difference between the ALS- 373
 derived PCDs and simulated high flow. This implies a potential 374
 for inferring high-flow direction from ALS-derived PCD for 375
 this area. However, an area with notable discrepancies of the 376
 ALS-derived PCDs and high-flow direction is also presented 377
 [denoted as rectangle A in Fig. 5(a)]. For the temporarily 378
 submerged gravel bed area, we observed that the ALS-derived 379
 PCDs showed better agreement with the simulated low-flow 380
 direction than the high-flow direction [where a larger number 381
 of red and yellow segments are found in Fig. 5(b)], except for 382
 the rectangle B area. 383

Furthermore, Fig. 4 reveals that the angle differences at high 384
 flow exhibit a peak close to 0° , while at low flow, the peak is 385
 close to 30° , which suggests that the PCDs of bed surface struc- 386
 ture are, overall, better correlated to the high flow. However, for 387
 the topographically low spots (e.g., rectangle B in Fig. 5), the 388
 low flow might have left a signature on the bed surface during 389
 the recession of flood, where the PCDs are better correlated 390
 to the low flow. From the aforementioned results, we demon- 391
 strated that the ALS-derived PCDs correspond to the flow 392
 directions at different flow rates. 393

It is noted that the typhoon-induced torrents were 3-D turbu- 394
 lent flows, typically characterized by fluctuating velocities with 395
 their magnitudes and directions changing with time and depth 396
 [30]. However, the 2-D hydrodynamic simulation performed 397
 herein was based on steady depth-averaged flood flows; thus, 398
 the discrepancies between the PCDs of bed surface structure 399
 and the computed flow directions may be attributable in part to 400
 these unresolved spatial variations. 401

V. CONCLUSION

402

In summary, we have explored the relationship of the aniso- 403
 tropy direction of exposed gravel bed (i.e., the ALS-derived 404
 PCDs) and simulated flow directions. We have determined the 405
 PCDs from the 2DVSs by applying an ellipse-fitting procedure 406
 with consideration given to the grain size characteristic d_{50} . 407
 The angle differences between the ALS-derived PCDs and sim- 408
 ulated flow directions were calculated, and the Kruskal–Wallis 409
 test was performed on the angle differences. The results suggest 410
 that the ALS-derived PCDs estimated from any elliptical con- 411
 tour of the 2DVS should exhibit similar orientation when the 412
 contours of the 2DVS reveal a clear anisotropic structure. Fur- 413
 thermore, the comparison of the ALS-derived PCDs and sim- 414
 ulated flow directions shows good agreement, which suggests 415
 that ALS-derived PCDs could be used to infer flow direction at 416
 different flow rates. 417

What is remarkable here is that the process for determining 418
 the PCD in the 2DVS is largely automatic and is scalable. Here, 419
 we applied the technique to 324 ALS $6\text{ m} \times 6\text{ m}$ subsets, but 420
 potentially, this is expandable and scalable to the whole ALS 421
 scenes where the river can be adequately demarcated. Thus, this 422
 letter points to the potential of determining flow direction across 423
 large areas, at both high and low flow, without the need for 424
in situ measurement or simulation modeling. Future research 425
 should demonstrate this ability across a range of different flow 426
 conditions and for a wider range of gravel bed surfaces. 427

REFERENCES

- 428
- 429 [1] P. Goovaerts, *Geostatistics for Natural Resources Evaluation*. London,
430 U.K.: Oxford Univ. Press, 1997.
- 431 [2] R. Mott, M. Schirmer, and M. Lehning, "Scaling properties of wind
432 and snow depth distribution in an alpine catchment," *J. Geophys. Res.*
433 *Atmos.*, vol. 116, no. D6, Mar. 2011, Art. no. D06106, doi: 10.1029/
434 2010JD014886.
- 435 [3] J. Aberle and V. Nikora, "Statistical properties of armored gravel bed sur-
436 faces," *Water Resour. Res.*, vol. 42, no. 11, Nov. 2006, Art. no. W11414,
437 doi: 10.1029/2005WR004674.
- 438 [4] J. B. Butler, S. N. Lane, and J. H. Chandler, "Characterization of the struc-
439 ture of river-bed gravels using 2D fractal analysis," *Math. Geol.*, vol. 33,
440 no. 3, pp. 301–330, Apr. 2001.
- 441 [5] R. Hodge, J. Brasington, and K. Richards, "Analysing laser-scanned dig-
442 ital terrain models of gravel bed surfaces: Linking morphology to sedi-
443 ment transport processes and hydraulics," *Sedimentology*, vol. 56, no. 7,
444 pp. 2024–2043, May 2009.
- 445 [6] J. Qin, D. Zhong, G. Wangm, and S. L. Ng, "Influence of particle shape
446 on surface roughness: Dissimilar morphological structures formed by
447 man-made and natural gravels," *Geomorphology*, vol. 190, pp. 16–26,
448 May 2013.
- 449 [7] P. E. Carbonneau, S. N. Lane, and N. E. Bergeron, "Cost-effective
450 non-metric close-range digital photogrammetry and its application to a
451 study of coarse gravel river beds," *Int. J. Remote Sens.*, vol. 24, no. 14,
452 pp. 2837–2854, Jul. 2003.
- 453 [8] G.-H. Huang and C.-K. Wang, "Multi-scale geostatistical estimation
454 of gravel-bed roughness from terrestrial and airborne laser scanning,"
455 *IEEE Geosci. Remote Sens. Lett.*, vol. 9, no. 6, pp. 1084–1088,
456 Nov. 2012.
- 457 [9] P. K. Kitanidis, *Introduction to Geostatistics Applications in*
458 *Hydrogeology*. Cambridge, U.K.: Cambridge Univ. Press, 1997.
- 459 [10] J. Schlee, "Fluvial gravel fabric," *J. Sedimentary Petrol.*, vol. 27, no. 2,
460 pp. 162–176, 1957.
- 461 [11] D. J. Douglas, "The structure of sedimentary deposits of braided rivers,"
462 *Sedimentology*, vol. 1, no. 3, pp. 167–190, Sep. 1962.
- 463 [12] C. E. Johansson, "Orientation of pebbles in running water: A laboratory
464 study," *Geogr. Ann. A*, vol. 45, no. 2/3, pp. 85–112, 1963.
- 465 [13] G. Kelling and P. F. Williams, "Flume studies of the reorientation of
466 pebbles and shells," *J. Geol.*, vol. 75, no. 3, pp. 243–267, May 1967.
- 467 [14] B. R. Rust, "Pebble orientation in fluvial sediments," *J. Sedimentary*
468 *Petrol.*, vol. 42, no. 2, pp. 384–388, Jun. 1972.
- 469 [15] M. E. Kauffman and D. F. Ritter, "Cobble imbrication as a sensitive
470 indicator of subtle local changes in river flow direction," *Geology*, vol. 9,
471 no. 7, pp. 299–302, Jul. 1981.
- [16] R. P. Millane, M. I. Weir, and G. M. Smart, "Automated analysis of im- 472
brication and flow direction in alluvial sediments using laser-scan data," 473
J. Sedimentary Res., vol. 76, no. 8, pp. 1049–1055, Aug. 2006. 474
- [17] J. B. Laronne and M. A. Carson, "Interrelationships between bed mor- 475
phology and bed-material transport for a small, gravel-bed channel," 476
Sedimentology, vol. 23, no. 1, pp. 67–85, Feb. 1976. 477
- [18] S. Bertin and H. Friedrich, "Field application of close-range digital pho- 478
togrammetry (CRDP) for grain-scale fluvial morphology studies," *Earth* 479
Surf. Process. Landforms, to be published, doi: 10.1002/esp.3906. 480
- [19] G. Smart, J. Aberle, M. Duncan, and J. Walsh, "Measurement and analysis 481
of alluvial bed roughness," *J. Hydraulic Res.*, vol. 42, no. 3, pp. 227–237, 482
2004. 483
- [20] L. Mao, J. R. Cooper, and L. E. Frostick, "Grain size and topographical 484
differences between static and mobile armour layers," *Earth Surf. Process.* 485
Landforms, vol. 36, no. 10, pp. 1321–1334, Aug. 2011. 486
- [21] R. M. Westaway, S. N. Lane, and D. M. Hicks, "Remote survey of large- 487
scale braided, gravel-bed rivers using digital photogrammetry and image 488
analysis," *Int. J. Remote Sens.*, vol. 24, no. 4, pp. 795–815, 2003. 489
- [22] A. S. Woodget, P. E. Carbonneau, F. Visser, and I. P. Maddock, "Quantify- 490
ing submerged fluvial topography using hyperspatial resolution UAS im- 491
agery and structure from motion photogrammetry," *Earth Surf. Process.* 492
Landforms, vol. 40, no. 1, pp. 47–64, Jan. 2015. 493
- [23] A. D. Tamminga, B. C. Eaton, and C. H. Hugenholtz, "UAS-based remote 494
sensing of fluvial change following an extreme flood event," *Earth Surf.* 495
Process. Landforms, vol. 40, no. 11, pp. 1464–1476, Sep. 2015. 496
- [24] J. Hohenthal, P. Alho, J. Hyypä, and H. Hyypä, "Laser scanning appli- 497
cations in fluvial studies," *Progr. Phys. Geogr.*, vol. 35, no. 6, pp. 782–809, 498
Dec. 2011. 499
- [25] "Titan Multispectral Lidar System Datasheet," Teledyne Optech Inc., 500
Kiln, MS, USA, Accessed Mar. 15, 2016. [Online]. Available: [http://](http://www.teledyneoptech.com/wp-content/uploads/Titan-Specsheet-150515-WEB.pdf) 501
[www.teledyneoptech.com/wp-content/uploads/Titan-Specsheet-150515-](http://www.teledyneoptech.com/wp-content/uploads/Titan-Specsheet-150515-WEB.pdf) 502
[WEB.pdf](http://www.teledyneoptech.com/wp-content/uploads/Titan-Specsheet-150515-WEB.pdf) 503
- [26] E. H. Isaaks and R. M. Srivastava, *Applied Geostatistics*. New York, NY, 504
USA: Oxford Univ. Press, 1989. 505
- [27] D. J. Graham, S. P. Rice, and I. Reid, "A transferable method for the auto- 506
mated grain sizing of river gravels," *Water Resour. Res.*, vol. 41, Jul. 2005, 507
Art. no. W07020, doi: 10.1029/2004WR003868. 508
- [28] F.-C. Wu, Y.-C. Shao, and Y.-C. Chen, "Quantifying the forcing effect of 509
channel width variations on free bars: Morphodynamic modeling based 510
on characteristic dissipative Galerkin scheme," *J. Geophys. Res.*, vol. 116, 511
Sep. 2011, Art. no. F03023, doi: 10.1029/2010JF001941. 512
- [29] "Planning Report for Training of Upstream," Water Resour. Agency 513
(WRA), New Taipei, Taiwan, 2009. 514
- [30] J. S. Bridge, *Rivers and Floodplains: Forms, Processes, and Sedimentary* 515
Record. Hoboken, NJ, USA: Wiley-Blackwell, 2003. 516

AUTHOR QUERIES

AUTHOR PLEASE ANSWER ALL QUERIES

The paper exceeds the maximum allowable number of pages. Please shorten the paper to fit into five pages.

Please be aware that authors are required to pay overlength page charges (\$200 per page) if the paper is longer than 3 pages. If you cannot pay any or all of these charges please let us know.

This pdf contains 2 proofs. The first half is the version that will appear on Xplore. The second half is the version that will appear in print. If you have any figures to print in color, they will be in color in both proofs.

The “Open Access” option for your paper expires when the paper is published on Xplore in an issue with page numbers. Papers in “Early Access” may be changed to “Open Access.”

AQ1 = Please check if there is a need to change “expect” to “except.”

AQ2 = Please provide publication update in Ref. [18].

END OF ALL QUERIES

Anisotropy Characteristics of Exposed Gravel Beds Revealed in High-Point-Density Airborne Laser Scanning Data

Guo-Hao Huang, Chi-Kuei Wang, Fu-Chun Wu, and Peter M. Atkinson

Abstract—The aim of this study was to examine the relationship between the anisotropy direction of exposed gravel bed and flow direction. Previous studies have shown that the anisotropy direction of a gravel bed surface can be visually determined in the elliptical contours of 2-D variogram surface (2DVS). In this letter, airborne laser scanning (ALS) point clouds were acquired at a gravel bed, and the whole data set was divided into a series of $6\text{ m} \times 6\text{ m}$ subsets. To estimate the direction of anisotropy, we proposed an ellipse-fitting-based automatic procedure with consideration given to the grain size characteristic d_{50} to estimate the primary axis of anisotropy [hereafter referred to as the primary continuity direction (PCD)] in the 2DVS. The ALS-derived PCDs were compared to the flow directions (for both high and low flow) derived from hydrodynamic model simulation. Comparison of ALS-derived PCDs and simulated flow directions suggested that ALS-derived PCDs could be used to infer flow direction at different flow rates. Furthermore, we found that the ALS-derived PCDs estimated from any elliptical contour of the 2DVS exhibited a similar orientation when the contours of the 2DVS reveal the clear anisotropic structure, demonstrating the robustness of the technique.

Index Terms—Airborne laser scanning (ALS), flow direction, spatial continuity, 2-D variogram surface (2DVS).

I. INTRODUCTION

THE geostatistical variogram function has been recognized as an important tool for detecting spatial anisotropy in different variables, such as air pollution [1], snow depth [2], and exposed gravel bed structures [3]–[8]. The anisotropy indicates that the spatial correlation pattern changes with orientation, and it can be represented by the elliptical contours in a 2-D variogram surface (2DVS).

Many studies have shown that the visually determined anisotropy direction of a 2DVS can be associated with different mechanisms, such as wind for air pollution and snow depth structures [1], [2] and hydrodynamic dispersion (i.e., flow

movement) for homogeneous porous media [9]. In the last two decades, substantial studies have investigated the anisotropy directions derived from a 2DVS in the exposed gravel beds and suggested that the anisotropy directions exhibited in the gravel bed surfaces reflect the dominant grain orientation [3]–[6]. Various studies have examined the relationship between gravel orientation and flow direction [10]–[16]. For lower flows, larger pebbles, and lower pebble concentrations, elongated pebbles are transported by rolling and are deposited with their major axes normal to the flow direction. For higher flows, smaller pebbles, and higher pebble concentrations, the pebbles skip along the bed and tend to be deposited with their major axis parallel to the flow [16]. It has been reported that particle imbrication would occur naturally in a direction parallel to the flow [5], [16], [17]. Particle imbrication covering a range of directions might indicate that flow direction changed over the duration of the last competent event (e.g., varied with flow depth) or that different flows (with different directions) imbricated particles in different ways over time [16]. It has also been reported that the anisotropy directions failed at being conclusive on the surface-forming flow direction [5], [18]. The latter is notoriously difficult to determine accurately from *in situ* visual observations [19].

The determination of flow direction is essential to trace the water paths and sediment transportation. For coarse bed materials, rolling/sliding and saltation are the most possible modes of sediment transport, with rolling/sliding dominated by coarser pebbles and saltation dominated by finer gravel. Alignment of bed particles transverse to the flow can be associated with transport mode by rolling and sliding [17], while bed structure longitudinal to the flow can be attributed to deposition of saltating particles after contact with the upstream front of stable grain and particle imbrications [4], [5], [20]. It is thus of interest to explore the relationship between the anisotropy of gravel bed surfaces and flow direction across large areas. However, comparison of anisotropy direction determined visually from a 2DVS, extracted for laboratory and field gravel surfaces, to flow direction determined from subjective observation [3]–[6] revealed no common consensus about the relationship between anisotropy direction and flow movement in exposed gravel beds. This is possibly due to the limited numbers of data and the small spatial extents available to earlier researchers.

Advances in remote sensing have facilitated the measurement of gravel bed surfaces in a spatially extensive and cost-effective way based on the airborne approach, including airborne laser scanning (ALS), aerial photogrammetry, and unmanned aerial systems (UASs) [8], [21]–[23]. Huang and Wang [8] have indicated that a detailed description of gravel bed surfaces is

Manuscript received November 8, 2015; revised March 16, 2016 and April 11, 2016; accepted April 27, 2016.

G.-H. Huang and C.-K. Wang are with the Department of Geomatics, National Cheng Kung University, Tainan 70101, Taiwan (e-mail: chikuei@mail.ncku.edu.tw).

F.-C. Wu is with the Department of Bioenvironmental Systems Engineering, National Taiwan University, Taipei 10617, Taiwan.

P. M. Atkinson is with the Department of Geography and Environment, University of Southampton, SO17 1BJ Southampton, U.K., with the Faculty of Science and Technology, Lancaster University, Lancaster LA1 4YW, U.K., with the Faculty of Geosciences, University of Utrecht, 3584 Utrecht, The Netherlands, and also with the School of Geography, Archaeology and Palaeoecology, Queen's University, Belfast BT7 1NN, U.K.

Color versions of one or more of the figures in this paper are available online at <http://ieeexplore.ieee.org>.

Digital Object Identifier 10.1109/LGRS.2016.2562061

88 a prerequisite for visualizing the obvious anisotropy pattern in
 89 the 2DVS of gravel bed surfaces. Recent progress on combining
 90 UAS and structure-from-motion photogrammetry has gained
 91 attention for measuring submerged and dry gravel beds, and
 92 it has been shown that a digital elevation model (DEM) with
 93 a spatial resolution of a few centimeters can be achieved [22],
 94 [23]. However, the UAS has to be operated at a low altitude
 95 (i.e., lower than 100 m) for such a purpose, and this would be
 96 challenging when performing UAS surveys in river valleys. The
 97 ALS, which incorporates laser ranging, inertial measurement
 98 unit, and Global Positioning System technologies, has shown
 99 potential for mapping the surface elevation of a large area [24].
 100 Moreover, the pulse repetition frequencies of the commercial
 101 ALS systems have increased from 70 kHz in 2003 (as for the
 102 ALS used in this study) to 900 kHz in 2014 [25], which shows
 103 that the ALS is now economically favorable for capturing
 104 gravel bed surfaces with high-density ALS point clouds.

105 In this research, we examined the anisotropy characteristics
 106 of a very high-point-density ALS data of an exposed gravel
 107 bed by comparing its anisotropy direction with simulated flow
 108 directions under high- and low-flow scenarios based on fixed-
 109 bed hydrodynamic modeling. To better reveal the variation of
 110 the anisotropy characteristic within the river channel, the whole
 111 ALS data set was divided into a series of $6\text{ m} \times 6\text{ m}$ subsets,
 112 which results in 324 subsets of ALS point data. In order to
 113 consistently derive the anisotropy direction for each $6\text{ m} \times 6\text{ m}$
 114 subset, we devised an ellipse-fitting-based automatic procedure
 115 with the consideration of the grain size characteristic d_{50} , which
 116 is the median of particle size distribution, to determine the
 117 primary axis of anisotropy [hereafter, referred to as the primary
 118 continuity direction (PCD)] in the 2DVS.

119 II. METHOD

120 A. 2DVS

121 The variogram has been used widely to quantify the spatial
 122 variability in gravel bed surfaces [4], [5], [8]. The empirical
 123 variogram, which is half the mean squared difference between
 124 pairs of data points separated by the lag vector \mathbf{h} , can be
 125 expressed as

$$\hat{\gamma}(\mathbf{h}) = \frac{1}{2N(\mathbf{h})} \sum_{i=1}^{N(\mathbf{h})} [z(\mathbf{x}_i) - z(\mathbf{x}_i + \mathbf{h})]^2 \quad (1)$$

126 where $\hat{\gamma}(\mathbf{h})$ is the semivariance, the lag (distance and direction)
 127 vector \mathbf{h} is the separation between two data points, $N(\mathbf{h})$ is the
 128 number of point pairs separated by lag \mathbf{h} , and $z(\mathbf{x}_i)$ is the bed
 129 elevation at the location \mathbf{x}_i .

130 The empirical variogram is a function that relates semivari-
 131 ance $\hat{\gamma}(\mathbf{h})$ to lag \mathbf{h} and is usually expressed as a set of 1-D plots,
 132 where different plots represent different directions. An alterna-
 133 tive is to plot all directions together as a 2DVS, i.e., a raster map
 134 of semivariance values $\hat{\gamma}(\mathbf{h}_x, \mathbf{h}_y)$ representing the empirical
 135 variogram for all available lag vectors $\mathbf{h} = (\mathbf{h}_x, \mathbf{h}_y)$ [1], [26].

136 Previous studies suggested the removal of possible large-
 137 scale topographic trends (i.e., the bed slope), which causes the
 138 spatial basis in the collected spatial data, before calculation
 139 of the 2DVS [5]. In this research, the planar detrending was
 140 applied to each ALS $6\text{ m} \times 6\text{ m}$ subset, and the elevation
 141 residuals were used for calculation of the 2DVS.

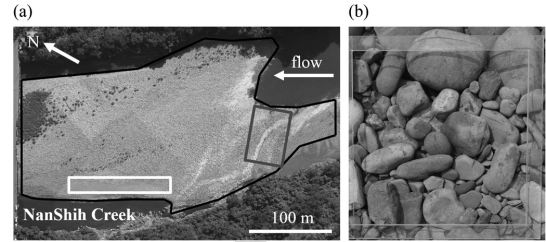


Fig. 1. (a) Georectified orthophoto with a spatial resolution of $5\text{ cm} \times 5\text{ cm}$ showing the gravel bar near the confluence of the NanShih Creek and PeiShih Creek, northern Taiwan, with a latitude of $24^\circ 54' 10''$ N and longitude of $121^\circ 33' 24''$ E. The black polygon shows the extent of exposed gravel bed. The gray rectangle represents a temporally submerged area caused by daily discharge fluctuations. The white rectangle represents an area that is covered by silt and gravel. (b) Image taken from the $50\text{ cm} \times 50\text{ cm}$ acrylic frame for photo-sieving.

142 B. Automatic Determination of Anisotropy Direction by 143 Ellipse Fitting

144 The 2DVS expressed as a contour plot can facilitate the
 145 analysis of spatial continuity (i.e., spatial autocorrelation) by
 146 visualizing the spatial variability along all directions simultane-
 147 ously [1], [26]. It is thus suggested that the anisotropy direction
 148 can be determined by tracing one of the elliptical contours in
 149 the 2DVS [26].

150 The procedure for determining the PCD is described as fol-
 151 lows. First, because the magnitude of the contours of the 2DVS
 152 is influenced by the actual semivariances $\hat{\gamma}(\mathbf{h}_x, \mathbf{h}_y)$, the semi-
 153 variances $\hat{\gamma}(\mathbf{h}_x, \mathbf{h}_y)$ in the 2DVS were standardized (divided by
 154 the variance of the elevation residuals for each ALS $6\text{ m} \times 6\text{ m}$
 155 subset), which implies that the contour levels in the 2DVS range
 156 theoretically between 0 and just greater than 1 (the maximum
 157 theoretical value is equal to the *a priori* variance not the sample
 158 variance). Then, we applied an ellipse-fitting procedure to all
 159 elliptical contours of the 2DVS such that the PCD, which rep-
 160 resents the direction of greatest spatial continuity (i.e., spatial
 161 autocorrelation), is estimated as the direction of the major axis
 162 of the fitted ellipse. Since the number of available contour levels
 163 in the 2DVS is inherently affected by the spatial autocorrelation
 164 property of the subject under investigation (in our case, the ALS
 165 point cloud of an exposed gravel bed), this raises difficulties in
 166 choosing the contour with a specific contour level for each ALS
 167 $6\text{ m} \times 6\text{ m}$ subset. As a result, the PCD is determined when the
 168 semimajor length of fitted ellipses falls in a given range derived
 169 by the grain size characteristic d_{50} . We chose the d_{50} value
 170 as a physically based guidance in the ellipse-fitting procedure,
 171 rather than an arbitrary measurement value, with the hope to
 172 maximize the transferability of this procedure to other study
 173 areas. The test results for determining the range constraint are
 174 shown in section *Determination of ALS-derived PCDs*.

175 III. DATA

176 The study area [Fig. 1(a)] is an exposed gravel bed (denoted
 177 as the black polygon) near the confluence of the NanShih
 178 Creek and PeiShih Creek, northern Taiwan, with latitude and
 179 longitude of $24^\circ 54' 10''$ N and $121^\circ 33' 24''$ E, respectively. The
 180 gravel bed was occasionally submerged and migrated by severe
 181 floods caused by typhoons that occurred between May and
 182 November of each year. It is noted that low discharges would
 183 temporarily cause a submerged area, which is denoted by the
 184 gray rectangle in Fig. 1(a).

185 Fig. 1(b) shows one of the 22 image samples, which were
 186 taken from the 50 cm \times 50 cm acrylic frame in the exposed
 187 gravel bed in Fig. 1(a). We applied the photo-sieving technique
 188 developed by Graham *et al.* [27] to derive the particle size
 189 distribution aggregated from the 22 image samples, and the
 190 resultant d_{50} is equal to 5.5 cm.

191 A. ALS

192 An ALS survey was conducted on May 7, 2009, at the above
 193 ground level of 650 m along the river channel using an Optech
 194 ALTM 3070 system onboard a helicopter with nominal eleva-
 195 tion and horizontal accuracies of 15 and 32.5 cm, respectively.
 196 The average point cloud density was 247 pts \cdot m⁻². Further-
 197 more, aerial photographs were also collected by a medium-
 198 format digital camera, integrated with an Optech ALTM 3070,
 199 simultaneously with laser scanning in order to generate georec-
 200 tified orthophotos with a spatial resolution of 5 cm \times 5 cm, as
 201 shown in Fig. 1(a).

202 For the ALS data of the exposed gravel bed, first, the extreme
 203 high points were removed manually. Then, the whole point data
 204 were divided into a series of 6 m \times 6 m subsets, each of which
 205 was aligned with the longitudinal and transverse directions in
 206 the mainstream of NanShih Creek. The mean spacing between
 207 the centers of 6 m \times 6 m subsets is 8 m. The specific 6 m \times 6 m
 208 subset size was chosen because our previous study [8] demon-
 209 strated that, using this size, reliable anisotropy patterns can
 210 be obtained for each subset while maximizing the number of
 211 available subsets. Furthermore, in order to avoid the potential
 212 bias caused by vegetation (sparse and short *Miscanthus*) on the
 213 gravel bed, we calculated the 2DVSs of ALS 6 m \times 6 m data
 214 sets only where the cumulative vegetation area was smaller than
 215 1 m² with the help of the 5-cm resolution orthophoto. This leads
 216 to 324 subsets available for 2DVS calculation.

217 The ALS data are also used to produce the DEM of the dry
 218 surfaces within the study area with a resolution of 1 m \times 1 m,
 219 where the point clouds belonging to vegetation were removed
 220 by visual inspection in Terrascan environment. Due to the in-
 221 frared wavelength of 1064 nm operated by the ALTM 3070,
 222 water absorption prevents ALS measurement for underwater
 223 surfaces. The underwater elevations were thus measured using
 224 a total station and surveying prism pole in wadable areas, while
 225 a shipboard single-beam SONAR was used to survey deeper
 226 areas in June 2009. To facilitate the integration of a complete
 227 DEM of the study area, all surveying, including ALS, was
 228 referenced to TWD97 datum, the national coordinate system
 229 of Taiwan. The DEMs of the wet surfaces of a resolution of
 230 1 m \times 1 m were interpolated from total station and SONAR
 231 data. The complete DEM of the study area was created by
 232 mosaicking the two DEMs of the dry and wet surfaces, respec-
 233 tively, and was further used for hydrodynamic modeling.

234 B. Hydrodynamic Modeling

235 To explore the relation between the ALS-derived PCDs and
 236 flow directions, we simulated the depth-averaged 2-D flow
 237 fields under high- and low-flow scenarios using a finite-element
 238 (FE) hydrodynamic model developed by Wu *et al.* [28]. The
 239 computational domain, extending 600 m to the Hsintien Creek
 240 and 700 and 500 m to the NanShih and PeiShih Creeks
 241 [Fig. 2(a)], contained 17105 elements and 9000 nodes with a

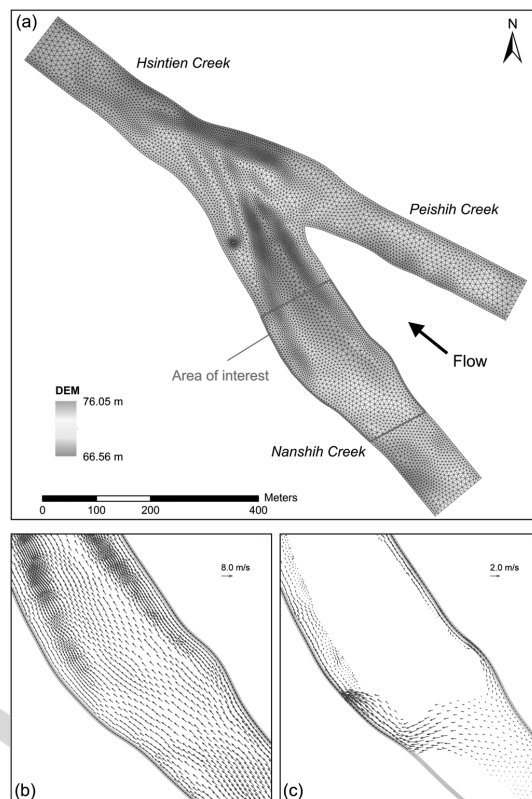


Fig. 2. (a) ALS-derived DEM map and computational mesh of simulation domain, which extends 600 m to the Hsintien Creek and 700 and 500 m to the NanShih and PeiShih Creeks, and contains 17105 elements and 9000 nodes with a mean spacing of 4 m; simulated velocity vectors under (b) high-flow and (c) low-flow scenarios, where the regions without velocity data are exposed bars. The scenario simulations exhibit different extents of bar submergence and distinct patterns of 2-D flow field.

mean spacing of 4 m. The ALS-derived DEM was mapped
 242 to the FE grids via a triangulated irregular network shown in
 243 Fig. 2(a). The model was validated with the observed water lev-
 244 els [29]. The calibrated parameter values were then used for the
 245 scenario simulations. The upstream boundary conditions (BC)
 246 were specified with the flows from the NanShih and PeiShih
 247 Creeks, while the downstream BC was specified with the water
 248 depth at the Hsintien Creek. For the high-flow scenario, the
 249 specified flows (3400 and 1230 m³s⁻¹) are equivalent to a flood
 250 event with seven-year return period; for the low-flow scenario,
 251 the specified values (23 and 18 m³s⁻¹) correspond to flows
 252 with a 50% probability of exceedance. These two scenario
 253 simulations exhibited different extents of bar submergence and
 254 distinct patterns of 2-D flow field [Fig. 2(b) and (c)]. The
 255 simulated velocity vectors at the FE nodes were interpolated
 256 to the centers of the 6 m \times 6 m ALS subset, allowing direct
 257 comparisons of the ALS-derived PCDs and flow directions. 258

IV. RESULTS AND DISCUSSION

A. Anisotropy Property of 2DVSs

The 2DVSs of the 324 ALS 6 m \times 6 m subsets were com-
 261 puted using the R software, and the contour map of the 2DVS
 262 was generated using a purpose-written MATLAB program. 263
 264 Based on internal testing, the lag distance of the 2DVS and the
 265 contour level interval in the contour plot were set to 15 cm and
 0.05, respectively, to best reveal anisotropic structures. 266

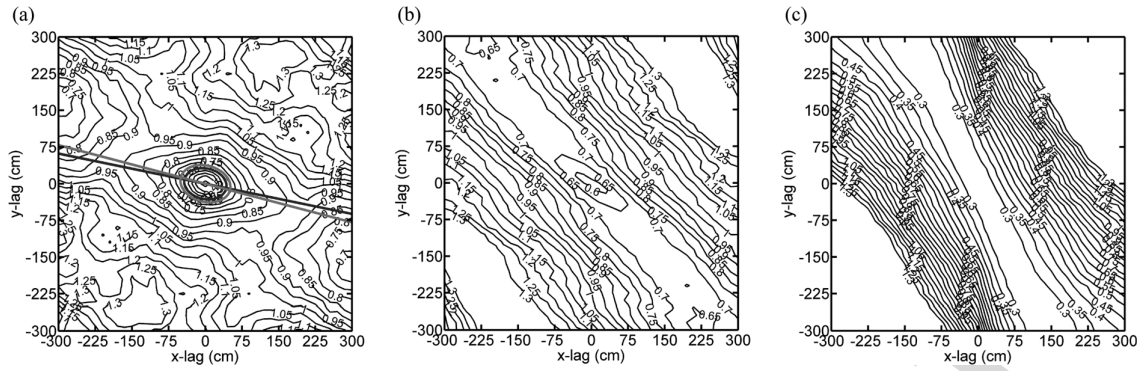


Fig. 3. (a) Contours of the 2DVS reveal a clear anisotropic structure. The ellipse-fitting procedure was applied to the black and gray contour, respectively, in order to determine the PCDs. The black and gray lines are the PCDs determined from the fitted ellipse with the semimajor axis lengths equal to $8.0 d_{50}$ and $9.5 d_{50}$, respectively. The contours of the 2DVS in (b) and (c) show a clear anisotropic structure, but there exist only parallel contours in (c), which prevents application of the ellipse-fitting procedure to obtain the PCD.

Most of the 2DVSs of the ALS $6\text{ m} \times 6\text{ m}$ subsets revealed a clear anisotropic structure similar to the contours shown in Fig. 3(a). It is thus appropriate to apply the ellipse-fitting procedure to a specific contour to determine the PCD. While a small number of subsets show fewer [Fig. 3(b)] or no [Fig. 3(c)] elliptical contours in their 2DVS, the anisotropic structure is still prominent. Based on visual inspection, the 2DVSs similar to Fig. 3(b) and (c) appeared to be in the area covered by silt and gravel, which is highlighted by the white rectangle in Fig. 1(a). Due to the requirement of ellipse fitting, the ALS-derived PCDs are only available for those 2DVSs similar to Fig. 3(a) and (b).

B. Determination of ALS-Derived PCDs

To mitigate the influence of the jagged appearance of the elliptical contours with small lag distances [c.f., Fig. 3(a)] on the PCD estimation, we applied the ellipse-fitting procedure only to those contour lines including more than 20 cells in the 2DVS, which implies that the semimajor axis length of the fitted ellipse should be larger than $7 d_{50}$ in our study area.

When there are more than two candidate contour lines that fall in a range of multiple times of d_{50} , we select the PCD with the smallest semimajor axis length. As shown in our data, the difference between different PCDs is insignificant. Fig. 3(a) shows an example for the determination of the PCD with the semimajor axis length constraint being $7\text{--}10 d_{50}$, and two candidate contours with their semimajor axis lengths of $8.0 d_{50}$ and $9.5 d_{50}$ [black line in Fig. 3(a)] and $9.5 d_{50}$ [gray line in Fig. 3(a)] were found, where the former one would be reported. The angle difference between these two PCDs is as small as 3° .

To further examine the insignificance of PCD bias caused by the choice of semimajor axis length constraint in the ellipse fitting, we generated three sets of ALS-derived PCDs determined from the semimajor axis length within three ranges, i.e., $7\text{--}10 d_{50}$, $9\text{--}12 d_{50}$, and $11\text{--}14 d_{50}$, and compared these PCD results with the simulated high- and low-flow directions. The choice of these constraint ranges was made in order to maximize of chance of having at least one available contour for each constraint.

C. Comparison of ALS-Derived PCDs and Simulated Flow Directions

The angle differences of the ALS-derived PCDs and simulated flow directions were calculated. The positive angle dif-

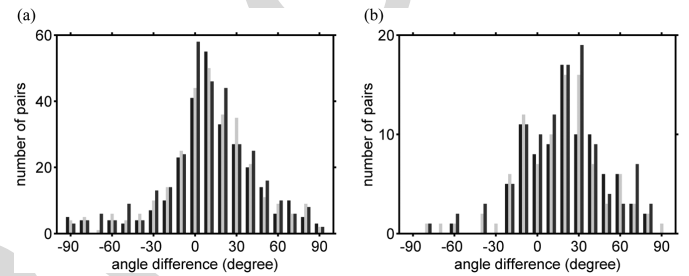


Fig. 4. Histograms of the angle differences between the three sets of ALS-derived PCDs and simulated flow directions at (a) high and (b) low flow. The red, green, and blue bins represent the histograms of the angle differences calculated from the three sets of ALS-derived PCDs determined by the semimajor axis length constraints, which are $7\text{--}10 d_{50}$, $9\text{--}12 d_{50}$, and $11\text{--}14 d_{50}$, respectively.

ferences denote that the ALS-derived PCD lies to the left of the simulated flow directions when facing downstream; the negative angle differences denote that the ALS-derived PCD lies to the right of the simulated flow directions.

The histograms of the angle differences for high and low flow are shown in Fig. 4(a) and (b), respectively. The red, green, and blue bins in Fig. 4 represent the histograms of the angle differences calculated from the three sets of ALS-derived PCDs determined by the semimajor axis length constraints being $7\text{--}10 d_{50}$, $9\text{--}12 d_{50}$, and $11\text{--}14 d_{50}$, respectively. For the high flow, the total numbers of comparison pairs are 324, 299, 317 and 275 when the semimajor axis constraints are $7\text{--}10 d_{50}$, $9\text{--}12 d_{50}$, and $11\text{--}14 d_{50}$, respectively; for the low flow, the total numbers of comparison pairs become 107, 96, and 89 when the semimajor axis constraints are $7\text{--}10 d_{50}$, $9\text{--}12 d_{50}$, and $11\text{--}14 d_{50}$, respectively. Because the submerged area is much smaller for low-flow condition [c.f., Fig. 2(c)], the number of comparison pairs for low flow was much less than that for high flow. Furthermore, we noted that the number of available ALS-derived PCDs decreased with the increase of the semimajor axis length constraint. Because the semivariances of 2DVS are expected to increase slowly at large lag distances [1], [26], the larger spacing of contours in the 2DVS leads to fewer contours available for ellipse fitting. As observed in Fig. 3(a), the elliptical contours starting from 0.5 to 0.9 become sparse. It is also noted that the contours became fragmented, and it was not easy to find ellipse shape [as shown in the upper left and lower right corner in Fig. 3(a)] when the data are not able to reveal such long range spatial correlation in the 2DVS.

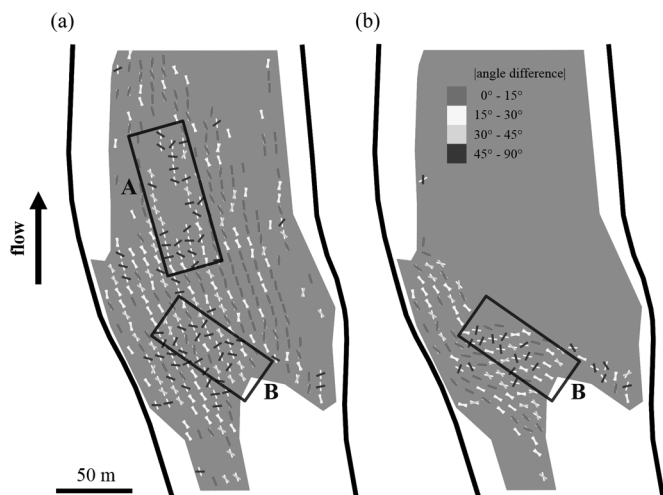


Fig. 5. Comparison of the ALS-derived PCDs and simulated flow directions at (a) high and (b) low flow. The gray polygon is the extent of the exposed gravel bed. The white segments represent the simulated flow directions. The red, yellow, green, and blue segments denote the absolute values of angle difference of $0^\circ-15^\circ$, $15^\circ-30^\circ$, $30^\circ-45^\circ$, and $45^\circ-90^\circ$, respectively, of the ALS-derived PCDs with respect to simulated flow directions. Rectangle A denotes the area with notable discrepancies of ALS-derived PCDs and high-flow direction. Rectangle B denotes the area where the ALS-derived PCDs have better agreement with low-flow direction than high-flow direction.

336 As observed in Fig. 4, the distributions of the angle differ-
 337 ences with three different semimajor axis constraints for high
 338 and low flow are, respectively, similar. To further demonstrate
 339 the similarity between each distribution of angle difference,
 340 for high and low flow, respectively, we applied the nonpara-
 341 metric Kruskal–Wallis test, implemented in R software. The
 342 null hypothesis for the Kruskal–Wallis test is that the three
 343 sets of angle differences come from the same distribution. The
 344 resultant p -values for the Kruskal–Wallis test are 0.89 and 0.83
 345 for high and low flow, respectively, both of which failed to reject
 346 the null hypothesis at the significant level of 0.05. This implies
 347 that the angle differences calculated from the three sets of
 348 ALS-derived PCDs and simulated flow directions do not reveal
 349 statistically significant differences. It is thus suggested that the
 350 ALS-derived PCDs derived from any elliptical contour of the
 351 2DVS should exhibit similar orientation when the contours
 352 of the 2DVS reveal the clear anisotropic structure. The ALS-
 353 derived PCDs determined with the semimajor axis length con-
 354 straint of $7-10 d_{50}$ are discussed as it gave the largest number
 355 of comparison pairs.

356 Fig. 5(a) and (b) demonstrates the comparison of ALS-
 357 derived PCDs and simulated high- and low-flow directions,
 358 respectively. The gray polygon in Fig. 5 shows the extent
 359 of exposed gravel bed [also shown as the black polygon in
 360 Fig. 1(a)]. The white segments in Fig. 5 represent the simulated
 361 flow directions. We observed that the simulated flow directions
 362 for high flow are primarily parallel to the main stream direc-
 363 tion in Fig. 5(a). Moreover, the simulated low flow primarily
 364 flows through the temporarily submerged area in Fig. 5(b)
 365 [c.f., the gray rectangle in Fig. 1(a)]. The red, yellow, green,
 366 and blue segments in Fig. 5 denote the absolute values of
 367 angle difference of $0^\circ-15^\circ$, $15^\circ-30^\circ$, $30^\circ-45^\circ$, and $45^\circ-90^\circ$,
 368 respectively, of the ALS-derived PCDs with respect to simu-
 369 lated flow directions.

We noted a good agreement between the ALS-derived PCDs 370
 and simulated high flow in the right portion of the exposed 371
 gravel bar [Fig. 5(a)], where the white segments become invis- 372
 ible due to the insignificant angle difference between the ALS- 373
 derived PCDs and simulated high flow. This implies a potential 374
 for inferring high-flow direction from ALS-derived PCD for 375
 this area. However, an area with notable discrepancies of the 376
 ALS-derived PCDs and high-flow direction is also presented 377
 [denoted as rectangle A in Fig. 5(a)]. For the temporarily 378
 submerged gravel bed area, we observed that the ALS-derived 379
 PCDs showed better agreement with the simulated low-flow 380
 direction than the high-flow direction [where a larger number 381
 of red and yellow segments are found in Fig. 5(b)], except for 382
 the rectangle B area. 383

Furthermore, Fig. 4 reveals that the angle differences at high 384
 flow exhibit a peak close to 0° , while at low flow, the peak is 385
 close to 30° , which suggests that the PCDs of bed surface struc- 386
 ture are, overall, better correlated to the high flow. However, for 387
 the topographically low spots (e.g., rectangle B in Fig. 5), the 388
 low flow might have left a signature on the bed surface during 389
 the recession of flood, where the PCDs are better correlated 390
 to the low flow. From the aforementioned results, we demon- 391
 strated that the ALS-derived PCDs correspond to the flow 392
 directions at different flow rates. 393

It is noted that the typhoon-induced torrents were 3-D turbu- 394
 lent flows, typically characterized by fluctuating velocities with 395
 their magnitudes and directions changing with time and depth 396
 [30]. However, the 2-D hydrodynamic simulation performed 397
 herein was based on steady depth-averaged flood flows; thus, 398
 the discrepancies between the PCDs of bed surface structure 399
 and the computed flow directions may be attributable in part to 400
 these unresolved spatial variations. 401

V. CONCLUSION

402

In summary, we have explored the relationship of the aniso- 403
 tropy direction of exposed gravel bed (i.e., the ALS-derived 404
 PCDs) and simulated flow directions. We have determined the 405
 PCDs from the 2DVSs by applying an ellipse-fitting procedure 406
 with consideration given to the grain size characteristic d_{50} . 407
 The angle differences between the ALS-derived PCDs and sim- 408
 ulated flow directions were calculated, and the Kruskal–Wallis 409
 test was performed on the angle differences. The results suggest 410
 that the ALS-derived PCDs estimated from any elliptical con- 411
 tour of the 2DVS should exhibit similar orientation when the 412
 contours of the 2DVS reveal a clear anisotropic structure. Fur- 413
 thermore, the comparison of the ALS-derived PCDs and sim- 414
 ulated flow directions shows good agreement, which suggests 415
 that ALS-derived PCDs could be used to infer flow direction at 416
 different flow rates. 417

What is remarkable here is that the process for determining 418
 the PCD in the 2DVS is largely automatic and is scalable. Here, 419
 we applied the technique to 324 ALS $6\text{ m} \times 6\text{ m}$ subsets, but 420
 potentially, this is expandable and scalable to the whole ALS 421
 scenes where the river can be adequately demarcated. Thus, this 422
 letter points to the potential of determining flow direction across 423
 large areas, at both high and low flow, without the need for 424
in situ measurement or simulation modeling. Future research 425
 should demonstrate this ability across a range of different flow 426
 conditions and for a wider range of gravel bed surfaces. 427

REFERENCES

- 428
- 429 [1] P. Goovaerts, *Geostatistics for Natural Resources Evaluation*. London,
430 U.K.: Oxford Univ. Press, 1997.
- 431 [2] R. Mott, M. Schirmer, and M. Lehning, "Scaling properties of wind
432 and snow depth distribution in an alpine catchment," *J. Geophys. Res.*
433 *Atmos.*, vol. 116, no. D6, Mar. 2011, Art. no. D06106, doi: 10.1029/
434 2010JD014886.
- 435 [3] J. Aberle and V. Nikora, "Statistical properties of armored gravel bed sur-
436 faces," *Water Resour. Res.*, vol. 42, no. 11, Nov. 2006, Art. no. W11414,
437 doi: 10.1029/2005WR004674.
- 438 [4] J. B. Butler, S. N. Lane, and J. H. Chandler, "Characterization of the struc-
439 ture of river-bed gravels using 2D fractal analysis," *Math. Geol.*, vol. 33,
440 no. 3, pp. 301–330, Apr. 2001.
- 441 [5] R. Hodge, J. Brasington, and K. Richards, "Analysing laser-scanned dig-
442 ital terrain models of gravel bed surfaces: Linking morphology to sedi-
443 ment transport processes and hydraulics," *Sedimentology*, vol. 56, no. 7,
444 pp. 2024–2043, May 2009.
- 445 [6] J. Qin, D. Zhong, G. Wangm, and S. L. Ng, "Influence of particle shape
446 on surface roughness: Dissimilar morphological structures formed by
447 man-made and natural gravels," *Geomorphology*, vol. 190, pp. 16–26,
448 May 2013.
- 449 [7] P. E. Carbonneau, S. N. Lane, and N. E. Bergeron, "Cost-effective
450 non-metric close-range digital photogrammetry and its application to a
451 study of coarse gravel river beds," *Int. J. Remote Sens.*, vol. 24, no. 14,
452 pp. 2837–2854, Jul. 2003.
- 453 [8] G.-H. Huang and C.-K. Wang, "Multi-scale geostatistical estimation
454 of gravel-bed roughness from terrestrial and airborne laser scanning,"
455 *IEEE Geosci. Remote Sens. Lett.*, vol. 9, no. 6, pp. 1084–1088,
456 Nov. 2012.
- 457 [9] P. K. Kitanidis, *Introduction to Geostatistics Applications in*
458 *Hydrogeology*. Cambridge, U.K.: Cambridge Univ. Press, 1997.
- 459 [10] J. Schlee, "Fluvial gravel fabric," *J. Sedimentary Petrol.*, vol. 27, no. 2,
460 pp. 162–176, 1957.
- 461 [11] D. J. Douglas, "The structure of sedimentary deposits of braided rivers,"
462 *Sedimentology*, vol. 1, no. 3, pp. 167–190, Sep. 1962.
- 463 [12] C. E. Johansson, "Orientation of pebbles in running water: A laboratory
464 study," *Geogr. Ann. A*, vol. 45, no. 2/3, pp. 85–112, 1963.
- 465 [13] G. Kelling and P. F. Williams, "Flume studies of the reorientation of
466 pebbles and shells," *J. Geol.*, vol. 75, no. 3, pp. 243–267, May 1967.
- 467 [14] B. R. Rust, "Pebble orientation in fluvial sediments," *J. Sedimentary*
468 *Petrol.*, vol. 42, no. 2, pp. 384–388, Jun. 1972.
- 469 [15] M. E. Kauffman and D. F. Ritter, "Cobble imbrication as a sensitive
470 indicator of subtle local changes in river flow direction," *Geology*, vol. 9,
471 no. 7, pp. 299–302, Jul. 1981.
- [16] R. P. Millane, M. I. Weir, and G. M. Smart, "Automated analysis of im- 472
brication and flow direction in alluvial sediments using laser-scan data," 473
J. Sedimentary Res., vol. 76, no. 8, pp. 1049–1055, Aug. 2006. 474
- [17] J. B. Laronne and M. A. Carson, "Interrelationships between bed mor- 475
phology and bed-material transport for a small, gravel-bed channel," 476
Sedimentology, vol. 23, no. 1, pp. 67–85, Feb. 1976. 477
- [18] S. Bertin and H. Friedrich, "Field application of close-range digital pho- 478
togrammetry (CRDP) for grain-scale fluvial morphology studies," *Earth* 479
Surf. Process. Landforms, to be published, doi: 10.1002/esp.3906. 480
- [19] G. Smart, J. Aberle, M. Duncan, and J. Walsh, "Measurement and analysis 481
of alluvial bed roughness," *J. Hydraulic Res.*, vol. 42, no. 3, pp. 227–237, 482
2004. 483
- [20] L. Mao, J. R. Cooper, and L. E. Frostick, "Grain size and topographical 484
differences between static and mobile armour layers," *Earth Surf. Process.* 485
Landforms, vol. 36, no. 10, pp. 1321–1334, Aug. 2011. 486
- [21] R. M. Westaway, S. N. Lane, and D. M. Hicks, "Remote survey of large- 487
scale braided, gravel-bed rivers using digital photogrammetry and image 488
analysis," *Int. J. Remote Sens.*, vol. 24, no. 4, pp. 795–815, 2003. 489
- [22] A. S. Woodget, P. E. Carbonneau, F. Visser, and I. P. Maddock, "Quantify- 490
ing submerged fluvial topography using hyperspatial resolution UAS im- 491
agery and structure from motion photogrammetry," *Earth Surf. Process.* 492
Landforms, vol. 40, no. 1, pp. 47–64, Jan. 2015. 493
- [23] A. D. Tamminga, B. C. Eaton, and C. H. Hugenholtz, "UAS-based remote 494
sensing of fluvial change following an extreme flood event," *Earth Surf.* 495
Process. Landforms, vol. 40, no. 11, pp. 1464–1476, Sep. 2015. 496
- [24] J. Hohenthal, P. Alho, J. Hyypä, and H. Hyypä, "Laser scanning appli- 497
cations in fluvial studies," *Progr. Phys. Geogr.*, vol. 35, no. 6, pp. 782–809, 498
Dec. 2011. 499
- [25] "Titan Multispectral Lidar System Datasheet," Teledyne Optech Inc., 500
Kiln, MS, USA, Accessed Mar. 15, 2016. [Online]. Available: [http://](http://www.teledyneoptech.com/wp-content/uploads/Titan-Specsheet-150515-502)
501 [www.teledyneoptech.com/wp-content/uploads/Titan-Specsheet-150515-](http://www.teledyneoptech.com/wp-content/uploads/Titan-Specsheet-150515-502)
502 [WEB.pdf](http://www.teledyneoptech.com/wp-content/uploads/Titan-Specsheet-150515-502) 503
- [26] E. H. Isaaks and R. M. Srivastava, *Applied Geostatistics*. New York, NY, 504
USA: Oxford Univ. Press, 1989. 505
- [27] D. J. Graham, S. P. Rice, and I. Reid, "A transferable method for the auto- 506
mated grain sizing of river gravels," *Water Resour. Res.*, vol. 41, Jul. 2005, 507
Art. no. W07020, doi: 10.1029/2004WR003868. 508
- [28] F.-C. Wu, Y.-C. Shao, and Y.-C. Chen, "Quantifying the forcing effect of 509
channel width variations on free bars: Morphodynamic modeling based 510
on characteristic dissipative Galerkin scheme," *J. Geophys. Res.*, vol. 116, 511
Sep. 2011, Art. no. F03023, doi: 10.1029/2010JF001941. 512
- [29] "Planning Report for Training of Upstream," Water Resour. Agency 513
(WRA), New Taipei, Taiwan, 2009. 514
- [30] J. S. Bridge, *Rivers and Floodplains: Forms, Processes, and Sedimentary* 515
Record. Hoboken, NJ, USA: Wiley-Blackwell, 2003. 516

AUTHOR QUERIES

AUTHOR PLEASE ANSWER ALL QUERIES

The paper exceeds the maximum allowable number of pages. Please shorten the paper to fit into five pages.

Please be aware that authors are required to pay overlength page charges (\$200 per page) if the paper is longer than 3 pages. If you cannot pay any or all of these charges please let us know.

This pdf contains 2 proofs. The first half is the version that will appear on Xplore. The second half is the version that will appear in print. If you have any figures to print in color, they will be in color in both proofs.

The “Open Access” option for your paper expires when the paper is published on Xplore in an issue with page numbers. Papers in “Early Access” may be changed to “Open Access.”

AQ1 = Please check if there is a need to change “expect” to “except.”

AQ2 = Please provide publication update in Ref. [18].

END OF ALL QUERIES